Monograph:
Zhao, Y., Billings, S.A. and Routh, A.F. (2005) Identification of the Belousov-Zhabotinsky Reaction using Cellular Automata Models. Research Report. ACSE Research Report 910 . Department of Control Engineering, University of Sheffield

Identification of the Belousov-Zhabotinsky Reaction using Cellular Automata Models

Y. Zhao, S.A. Billings and Alexander F. Routh

Research Report No. 910

Department of Automatic Control and Systems Engineering
The University of Sheffield
Mappin Street, Sheffield,
S1 3JD, UK

November, 2005

Identification of the Belousov-Zhabotinsky Reaction using Cellular Automata Models

Y.Zhao, S.A.Billings [*], Alexander F.Routh[†]

November 24, 2005

Abstract

New methods of identifying the transition rule of a Belousov-Zhabotinsky (BZ) reaction directly from experimental data using cellular automata (CA) models are investigated. The experimental set-up and new techniques for image pre-processing to ensure the identification of representative models are discussed including noise reduction, pixel and colour calibration. Two kinds of models, the Greenberg-Hasting model (GHM) and the polynomial CA model are studied in detail. It is shown that the results of identifying a real BZ reacting system are very encouraging and the predicted patterns compare well with the imaged patterns both visually and quantitatively.

1 Introduction

The Belousov-Zhabotinsky (BZ) chemical reaction, named after B.P.Belousov who first discovered the reaction [1] and A.M.Zhabotinsky who continued Belousov's early work [2], is a famous experiment in excitable media. Excitable media like the BZ reaction represent an important class of spatio-temporal system, and are spatially extended systems that support solitary waves that propagate unattenuated over a wide spatial domain. Examples of excitable media include nerve and muscle tissue in living organisms [3]-[4], chemical reaction systems [5], ecological processes [7], and the aggregation of slime

[*]Department of Automatic Control and System Engineering, University of Sheffield, UK.
[†]Department of Chemical and Process Engineering, University of Sheffield, UK.

models [8]. Because of the simplicity of the models and the complexity of the generated pattern, excitable media have received increasing attention in the field of spatio-temporal systems because of the possibility of making straightforward analogies between real excitable media systems, partial differential equation models (PDE) (reaction-diffusion equations) and cellular automata (CA). However, only a few investigations have studied the inverse problem, that is how to extract mathematical models directly from real excitable media systems. Solving such problems would fill the gap in the identification of spatio-temporal systems and would open the possibility of controlling the output of such real systems.

In the present paper the identification of a model of a real BZ reaction using a CA model directly from sampled data will be studied. The focus of the paper will be on the practical aspects of imaging a real BZ reaction and the identification of dynamic models of this system because there are very few results on these type of problems in the literature. The study begins with the set-up of the BZ chemical experiment and the acquisition of the reaction patterns over time. Two methods of identifying the underlying rule based on the Greenberg-Hasting model (GHM) and a polynomial model realisation of CA are then introduced to describe the evolution characteristics of the BZ patterns.

The paper is organized as follows. The brief description of excitable media systems using a CA model is presented in section 2. Section 3 provides an overview of the BZ chemical experiment set-up and the data acquisition system. Pre-processing, calibration and the identification and evaluation of the rules to describe the observed patterns are discussed in section 4. Finally, conclusions are given in section 5.

2 CA Models of Excitable Media

Cellular automata (CA) are a class of spatially and temporally discrete mathematical systems characterized by local interactions which can be used to model excitable media. Because of the simple mathematical constructs and distinguishing features, CA have been widely used to model aspects of advanced computation, evolutionary computation, and for simulating a wide variety of complex systems in the real world [9], [10], [11] and [12].

A cellular automata is composed of three parts: a neighbourhood, a local transition rule and a discrete lattice structure. The local transition rule updates all cells synchronously by assigning to each cell, at a given step, a value that depends only on the neighbourhood.

Many CA models have been studied over the years for modelling excitable media, the most famous of which is the Greenberg-Hasting Model (GHM). The GHM, introduced by Greenberg and Hasting [13], was initially used to model neuron excitation and recovery in a network of neurons based on the excited-refractory-excitable definition, but currently, it has been expanded and used in modelling most kinds of excitable media, such as the Belousov-Zhabotinsky system. To assist in solving the inverse problem - that is to identify a model from observed data, this paper starts by investigating how the GHM can generate the patterns whose evolution characteristics are similar to those of the BZ reaction.

The GHM with an output pattern γ_t is a very simple cellular automata that emulates excitable media [14]. At each time t, $\gamma_t \in \{0, ..., N-1\}^{\mathbb{Z}^d}$. This means that for each $x \in \mathbb{Z}^d$, $\gamma_t(x)$ has one of N possible values $0, ..., N-1$, which appear as different colours in computer simulations, so they are usually referred to as *colours*. Recalling the components of CA, each site of a two-dimensional grid of the GHM at time t is assigned a state $\gamma_t(x, y)$, where x and y denote the location in the grid. The GHM evolution can be determined by three parts: a discrete lattice, a finite neighbourhood $\mathcal{R}$, and a transition rule. The commonly used lattice types for excitable media are illustrated in Figure 1. In this paper only the square lattice will be considered. The neighbourhood of a cell is the set of cells in both the spatial and temporal dimensions that are directly involved in the evolution of this cell. Typical neighbourhood types of excitable media are shown in Figure 2. The transition rule of a GHM can be determined by three parameters: the number N of all available colours; the number E of excited colours; and the threshold number T of sites needed for excitation. Denoting the cell at position (x, y) at time step t as $c(x; y; t)$. The state $c(x; y; t)(c(x; y; t) \in \{0, ..., N-1\})$ is an integer value, where 0 represents an excitable state, $1, ..., E$ represent the excited states, and $E+1, ..., N-1$ represent the refractory states. Initializing each cell at time step 0, the GHM updates

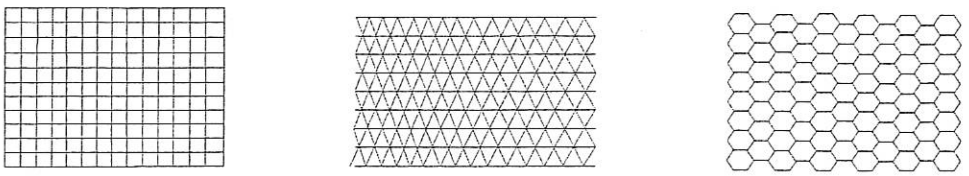

(a) (b) (c)

Figure 1: Lattice types of CA for excitable media. (a) square lattice; (b)triangular lattice; (c) hexagonal lattice

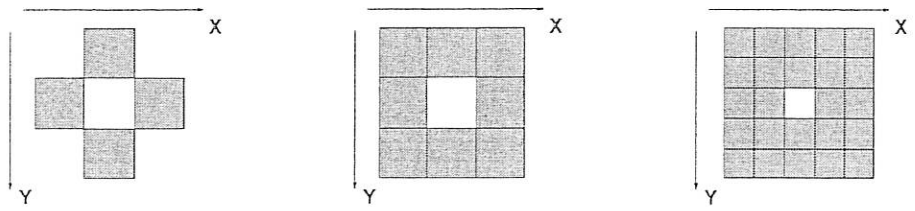

(a) (b) (c)

Figure 2: Neighbourhood structure types of CA for excitable media. (a)von Neumann structure; (b)Moore structure; (c) Extended Moore structure($r = 2$)

all cells synchronously by

$$c(x;y;t+1) = \begin{cases} (c(x;y;t)+1) \bmod \mathrm{N} & 1 \leq c(x;y;t) < N \\ 1 & c(x;y;t) = 0 \text{ and } \#(\mathcal{R}_{c(x;y;t)}) \geq T \\ 0 & \text{else} \end{cases} \quad (1)$$

where ($\#(\mathcal{R})$ denotes the number of excited sites in $\mathcal{R}$, and $\mathcal{R}$ denotes the neighbourhood of $c(x;y;t)$).

Using this simple rule, different complex patterns with rings and spirals, some snapshots of which are illustrated in Figure 3, can be generated when different initial values or parameters are used. More information about the lattice, neighbourhood and rules can be found in [15]. The main aim of this paper is to identify a model to represent the evolution characteristics of a BZ system using Expression (1) by estimating N, T and E directly from the observed patterns of the reaction. Furthermore, an algorithm using a polynomial model to describe the BZ patterns is also presented using recent research results for the identification of binary CA [16]-[18].

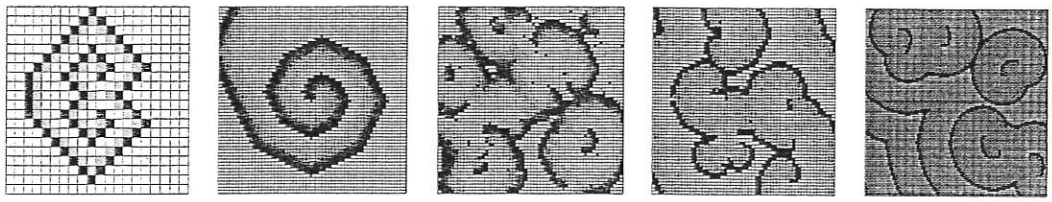

(a) (b) (c) (d) (e)

Figure 3: Snapshots generated by five different GHM models for simulating excitable media.

3 Experiment Design

3.1 Recipe

The chemical processor was prepared in a thin layer BZ reaction using a recipe adapted from Field and Winfree [6]:" *To 67 ml of water, add 2 ml of concentrated sulfuric acid and 5 gm of sodium bromate (total 70 ml). To 6ml of this in a glass vessel, add 1 ml of malonic acid solution (1 g per 10 ml). Add 0.5 ml of sodium bromide solution (1 g in 10 ml) and wait for the bromine color to vanish. Add 1 ml of 25 mM phenanthroline ferrous sulfate and a drop of Triton X-100 surfactant solution (1 g in 1000 ml) to facilitate spreading. Mix well, pour into a covered 90 ml Petri dish illuminated from below.*"
Once the reaction gets started grey rings and spirals can be seen propagating from localized regions on a red background. A snapshot of a typical pattern is shown in Figure 4.(c), where the wave fronts of the observed patterns appear to be quite similar to those of the simulated patterns using the GHM, especially the pattern shown in Figure 3.(e).

3.2 Data Acquisition

The experimental apparatus of acquisition is illustrated by Figure 4.(a). To acquire the high quality images a digital camera, which was fixed by a bracket and connected to the computer directly using the USB socket as shown in Figure 4.(b), was used. Operating at full speed, the camera could record at roughly 25 fps (frames per second) with 640×480 resolution when using video mode and 1 fps when using single frame mode. Because of the higher image quality of the single frame capture compared with video (the edges of the patterns, which are quite important for identification of the wave fronts, were

always corrupted by high video compression), and the slow velocity of evolution of the BZ reaction, single frame mode was adapted in the present study.

To enhance the images of excitation dynamics and to prevent an inverted or reflected image of the camera in the dish, back lighting was used to illuminate the bottom of the reaction dish. The experiment should ideally be conducted in a darkened environment, because the interference of daylight can change the luminance of the acquired images, which can introduce problems in the following image processing. The images were stored on the computer from the camera using a USB 2.0 connection.

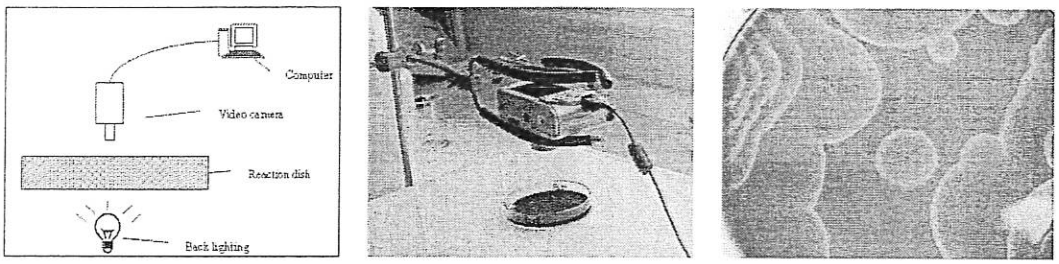

(a) (b) (c)

Figure 4: (a) Schematic of the data acquisition setup; (b) Photo of acquiring device ; (c)A snapshot of an acquired pattern

4 Data Processing and Identification of the Rule

The images were acquired with 640×480 pixel resolution where each pixel had a 24bit colour-scale value. Before identification the acquired raw data must be pre-processed to reduce noise and must then be mapped onto a lattice based on the three components of CA, which involves the calibration of the pixel size and the calibration of the number of colours.

4.1 Pre-processing

The purpose of this step is to reduce noise introduced by experimental devices and enhance the imaging of the wave fronts, which contain a majority of the evolution characteristics of the excitable state, refractory state and excited state. A pixel with 24bit colour-scale value can be divided into three parts: the red, green and blue components.

To determine which distribution efficiently characterizes the wave fronts, the pixels on a horizontal line were sampled, see Figure 5.(a). Figure 5.(b) shows the spatial distribution of each of the component values, and it is clear in this case that only the blue component of pixel colour can efficiently distinguish between the wave front and the background. Figure 5.(c) shows the blue component with the 8bit gray-scale value extracted from Figure 5.(a), and now most of the noise including the small bubbles on the bottom of the dish and the light spot in the right corner, have been effectively removed leaving the wave fronts highly enhanced.

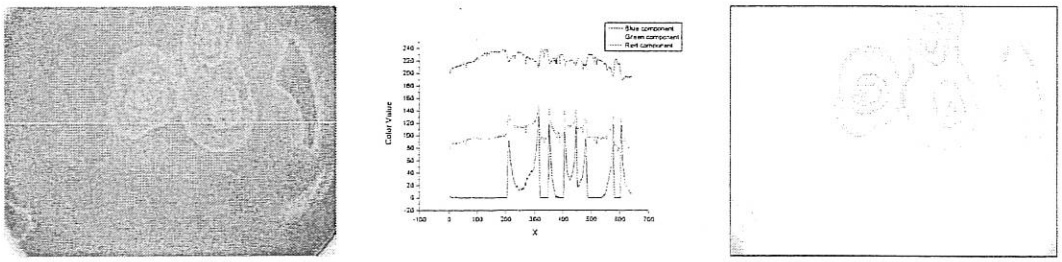

(a) (b) (c)

Figure 5: (a) A snapshot of the sampled image; (b) Values of the red, green and blue components along the raster shown in (a); (c) The blue component of the sampled image

4.2 Mapping to a Lattice

A point in a natural scene could be described by a rectangle of size 2×2 in a digitized image, or it could also be described by a rectangle of size 3×3 if a larger magnification was used. For example, in a CA simulation of a pattern a $n_1 \times n_2$ lattice size could be used and if the patterns were captured by a camera the size of the images in the camera could be $m_1 \times m_2$. The main goal of this step is to set up the relationship between the size of the captured image (e.g $m_1 \times m_2$) and the size of CA lattice (e.g $n_1 \times n_2$).
The calibration of the pixel size can be represented by:

$$k_c = \frac{\text{lattice pattern width}}{\text{raw image width}} \tag{2}$$

where $0 < k_c \leq 1$. If k_c is chosen too small, much important information, such as some thin wave fronts, could disappear and the identification can then never determine a correct model. If k_c is too big this may produce a large candidate neighbourhood, which

could lead to a failure in the identification because of insufficient sampled data (a larger neighbourhood will require more data to reveal the full complexity). With experience over several tests, $k_c = 0.60 \sim 0.98$ always seemed to produce a Moore neighbourhood, which is an ideal neighbourhood to generate a CA model in a real system without losing important wave fronts.

4.3 Colour Calibration

From section 2, the GHM has a parameter N which defines the total number of colours. It could be difficult to make a decision regarding how many colours should be used in the GHM from a pre-processed image. Fortunately, Expression (1) shows the cell in an excitable state (denoted by 0) transfers to an excited state (denoted by 1) at the next time step, all the other cells with other states $s_{x,y}$ say will update to state $s_{x,y} + 1$ unconditionally, and this will not be effected by the value of N. Hence, the selection of N does not have to be accurate. In our experiments, N was always chosen between 5 and 25.

After an appropriate value of N has been specified, the colour calibration procedure can be summarized by the following steps. *Initialization* Extract the blue component of the raw image, each cell of which has an 8bit gray-scale value, and then map the image to a latticed pattern, which will be denoted by R.

4.3.1 Horizontal Calibration

Extract the pixels on each horizontal line or raster R_y of R, where y denotes the vertical position. An example of R_y is illustrated by Figure 6, which shows that each positive segment denotes a wave front and the remaining gaps represent the background. A threshold value t_b was initially selected to distinguish between the wave front and the background. The pixels with the value above t_b can be averaged to N colours. The cells with peak values were set as the excited state and other cells were set as the refractory state.

The peak values of each positive segment are different, for example $p_1 = 92$ and $p_2 = 131$ in Figure 6. If a global calibration of colour is used, it could happen that the cell with value p_2 would be set as the excited state and the cell with value p_1 would be set as

the refractory state, which is unreasonable when considering the raw image, shown in Figure 5.(a). The difference in values between the two peaks may have been caused by a slightly different back-light or chemical density, but a visual inspection of Figure 5.(a) suggests that both these pixels should be in the excited state. Therefore, to remove the interference from the apparatus and the chemical material, a method using a local calibration of colour will be used in this paper.

Consider the line R_y and assume the peak value of the first positive segment is p_1 and the threshold value which distinguishes the wave fronts and the background is t_b. The value of the processed cell, denoted by $L_{x,y}$, can then be calculated by

$$L_{x,y} = \begin{cases} \frac{p_1 - v_{x,y}}{I_1} + 1 & \text{when } x_1 \leq x \leq x_2 \\ 0 & \text{else} \end{cases} \tag{3}$$

where x_1 and x_2 denote the front and back horizontal positions of the first wave front segment and $v_{x,y}$ denotes the value at the position (x, y) in R_y, and $I_1 = \frac{p_1 - t_b}{N}$ represents the calibration of colour of the first positive segment. As a simple example, the raw

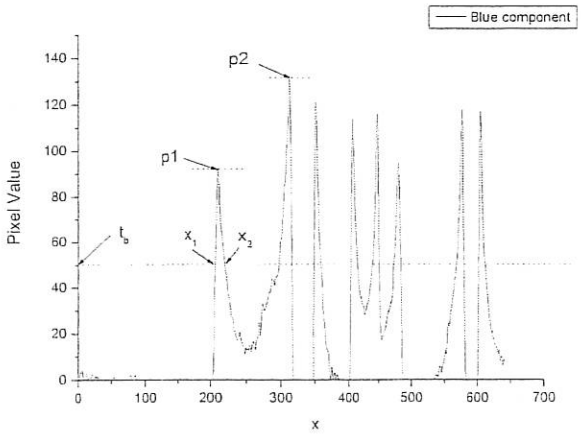

Figure 6: The blue component along the raster shown in Figure 5.(a)

image, shown in Figure 7.(a), will be used to illustrate this method. Inspection of the blue component of the bottom line in Figure 7.(a), Figure 7.(b), clearly shows two wave fronts could be extracted if t_b was set to be around 50. However, from Figure 7.(c), which illustrates the blue component of the top line in the raw image, two positive segments would be judged as one positive segment if $t_b = 50$. This would make some cells which

should be set as the excited state to be set as the refractory state in the top and bottom parts of the wave front (see Figure 8.(a)). In Figure 8.(a)-(d) green cells denote the excited states, grey cells denote the refractory states and white cells denote the excitable states. The main aim of t_b is to separate the wave fronts and the background, hence the selection of t_b depends on the luminance of the captured images. This is one of the reasons why the experiment should be conducted in a darkened environment, which should help to keep the luminance of images stable so that and t_b can be same through out the evolution.

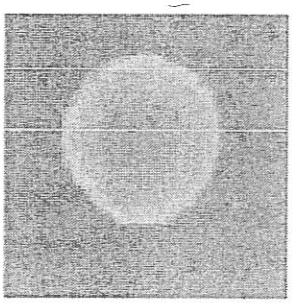

(a)

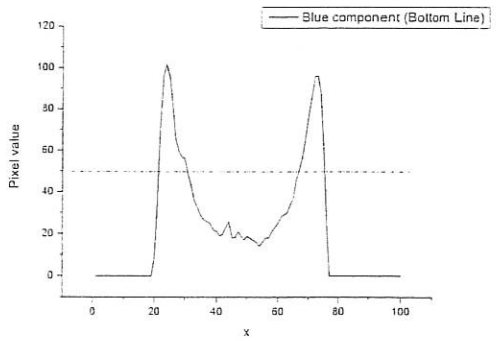

(b)

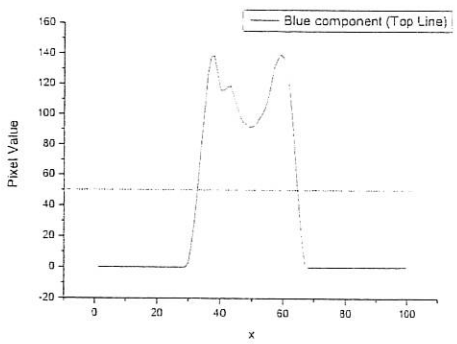

(c)

Figure 7: An example of colour calibration. (a) The raw image; (b) The blue component of the bottom line in (a); (c) The blue component of the top line in (a).

4.3.2 Vertical Calibration

To enhance the results of the horizontal calibration, a vertical calibration was also implemented. The procedure is the same as the horizontal calibration except now the data are

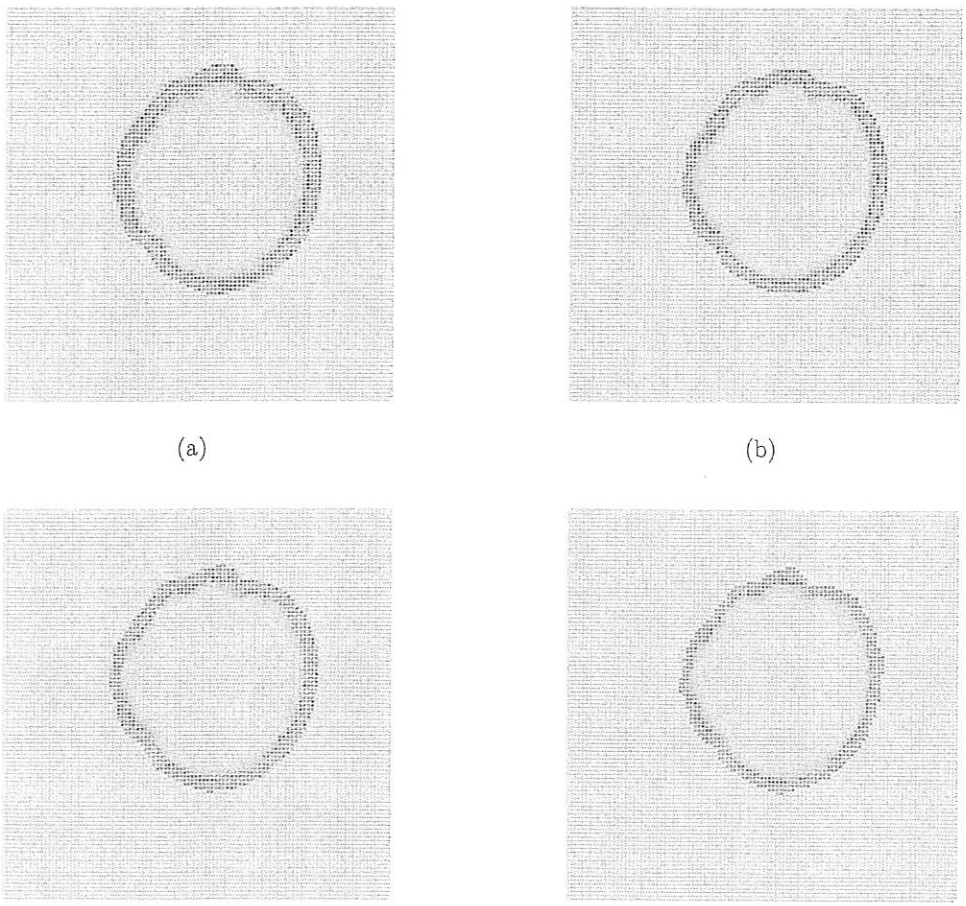

Figure 8: The results of colour calibration. (a) The processed pattern by horizontal colour calibration; (b) The processed pattern by vertical colour calibration; (c) The synthesized pattern by (a) and (b); (d) The final patterns after colour calibration;

extracted vertically. The processed image after vertical calibration is shown in Figure 8.(b).

4.3.3 Synthesize the Patterns and Edge Purging

Synthesized patterns were produced by combining the results from the horizontal and vertical calibration using the equation (4), where $c_h(x;y;t)$ and $c_v(x;y;t)$ denote the considered cell values produced by the horizontal and vertical calibration respectively, and $c_s(x;y;t)$ denotes the considered cell value in the synthesized pattern.

$$c_s(x;y;t) = \begin{cases} 1 & c_h(x;y;t) = 1 \text{ or } c_v(x;y;t) = 1 \\ max(c_h(x;y;t), c_v(x;y;t)) & \text{else} \end{cases} \quad (4)$$

Inspection of the synthesized pattern in Figure 8.(c) shows that the shape of the wave front is now clearly defined.

The bottom part of Figure 8.(c), which is shown more clearly in Figure 9.(a) shows that there are several cells below the excited cells which have refractory states following the diffusion direction of the wave front. This is unreasonable in excitable media because a cell in an excited or a refractory state will update to a refractory state or excitable state unconditionally, and therefore the wave front in Figure 8.(c) would not diffuse. To try and overcome this problem we developed a method to purge the redundant cells with refractory cells using the movement vector. The movement vector can be calculated using the techniques in [19]. Figure 9.(c) shows the movement vector of Figure 9.(a), and indicates that there are some cells at the bottom of the edge with remarkably different movement vectors, these are probably representative of the gradient between the wave front and the background. Therefore, the cells with refractory state with a direction opposite to the diffusion direction of the wave front were reset as excitable states. Figure 9.(b) shows the pattern after edge purging, and Figure 8.(d) illustrates the final CA pattern after all the calibration and pre-processing.

4.4 Rule Identification

4.4.1 Region Selection

In most recent studies of excitable media the evolution of the pattern is assumed to be uniform so that each cell in the pattern has the same transition rule. This may not hold for a real system because there may be noise introduced by data acquisition which could make the rule change. This could occur due to aberration at the edges of the image due to lens distortion or from imprecise timing during sampling etc. Hence, it is necessary to select an appropriate region of the image which has a uniform or nearly uniform rule Ideally, the rule of each cell should be calculated before applying region growing, a popular method in machine vision, to distinguish each region according to different rules. This method starts by choosing an arbitrary seed pixel which is then compared with neighbouring pixels according to similarity constraints. The region is then grown from the seed pixel if the neighbourhood pixels are similar. However, the disadvantage is that the procedure could result in an incorrect subset region when noise is introduced because

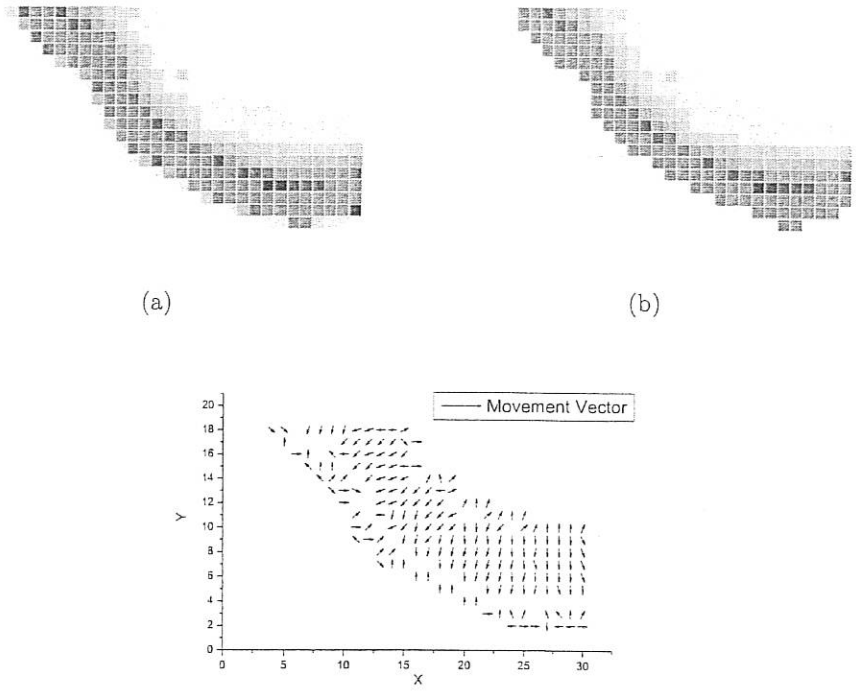

Figure 9: (a) The synthesized pattern without edge purging; (b) The synthesized pattern after edge purging; (c) The movement vector of pattern (a).

the growing would stop when the considered neighbouring pixels are noise corrupted and so do not satisfy the similarity constraints. We therefore devised a similar but simpler method which involves dividing the image into n_s squares, and then estimating the threshold number T in the GHM of each part. To provide a visional representation of this procedure the raw image was overlapped by a background colour where each colour represents a different T.

The precision of this method depends on the value of n_s. The larger n_s the more precise the region splitting, but with more susceptibility to noise. In this paper, n_s was chosen as 64 for a raw image with 640×480 pixels. An example is shown in Figure 10, where the white squares denote the background and the pink squares denote the area with the primary rule, and the areas with other colours may be corrupted by noise. Therefore, the framed region selected from the pink area was chosen as the sample region for the following analysis. There is little information in the literature on calibration and pre-processing but we have found that the methods we have introduced above are critical

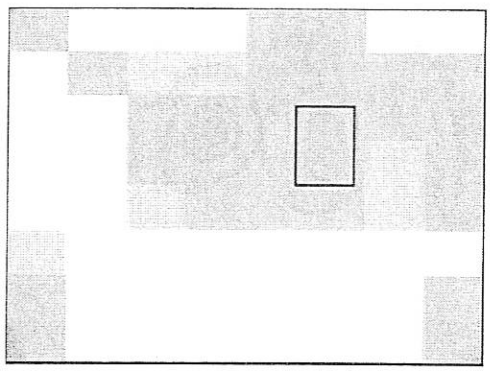

Figure 10: An example of region selection

for good pattern analysis and pure identification.

4.4.2 Rule Identification using the GHM

The evolution of a GHM is determined by four parameters: the neighbourhood; the number N of all available colours; the number E of excited colours; and the threshold number T of sites for excitation. The size of the neighbourhood can be influenced by the lattice calibration k_c. In this paper, the neighbourhood was restricted to a Moore structure and k_c was chosen as 0.95. As related parameters, N and E were specified as 13 and 3 respectively in the current experiment according to the discussion in 4.3. Therefore, T is the only parameter that needs to be estimated in this step.

To demonstrate the algorithm, 30 successive frames with 1fps sample rate were captured and sampled to provide the data for the identification. Figure 11.(a) and (b) show the 1^{st} and 30^{th} frame of the considered region of the raw images respectively, and Figure 11.(c) and (d) show the images after pre-processing, calibration and region selection. Consider a snapshot from the selected region at time step t_i and denote this frame as $P(t_i)$. Denote the cell at position (x, y) in $P(t_i)$ as $c(x; y; t_i)$, where $c(x; y; t_i) = 0$ represents an excitable state, $c(x; y; t_i) = 1..., E$ represent the excited states, and $c(x; y; t_i) = E + 1, ..., N - 1$ represent the refractory states. As shown in Equation (1), the cell $c(x; y; t_i)$ in an excited state or refractory state will update to $c(x; y; t_i) + 1 \bmod N$ unconditionally. Hence, the problem of identification of a GHM can be transformed into finding the rule when the considered cell $c(x; y; t_i)$ in an excitable state will be updated to an excited state at the next step time. Exploiting this observation the dimension of frame $P(t_i)$ can be

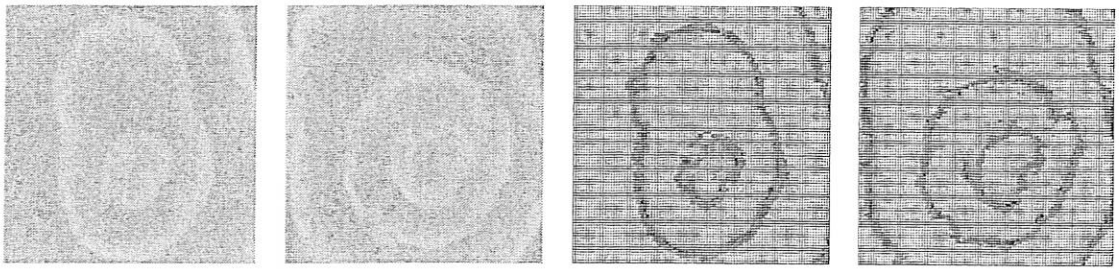

(a) (b) (c) (d)

Figure 11: (a) The 1^{st} frame; (b) The 30^{th} frame; (c) The latticed pattern of the 1^{st} frame; (d) The latticed pattern of the 30^{th} frame.

determined by thresholding and mapping this into a binary frame $P_b(t_i)$ following the rule:

$$c_b(x;y;t_i+1) = \begin{cases} 1 & 1 \leq c(x;y;t_i) \leq E \\ 0 & (E < c(x;y;t_i) < N) \text{ or } c(x;y;t_i) = 0 \end{cases} \quad (5)$$

where $c_b(x;y;t_i)$ is the cell at position (x,y) in $P_b(t_i)$.

Definition 1 *Consider a binary pattern generated by expression (5) and denote the cell at the position $(x;y)$ and at time step t as $c_b(x;y;t)$ and express the neighbourhood of $c_b(x;y;t)$ as $\mathcal{R}\{c_b(x;y;t)\}$. Assume the number of cells in $\mathcal{R}\{c_b(x;y;t)\}$ is n_c, for example, $n_c = 8$ when the neighbourhood is a Moore structure (see Figure 1.(b)). Define $s_{(i,j)}$ $(i \in \{0,1\}, j \in \{0,...,n_c\})$ as a counter. $s_{(i,j)}$ increases by 1 if a case is found such that $c_b(x;y;t+1) = i$ and the number of excited cells among the neighbourhood at time step t is j when $c_b(x;y;t) = 0$.*

A method for estimating T can now be summarized as:
Using the specified neighbourhood and E, a group of data $\{s_{(i,j)} : i \in \{0,1\}, j \in \{0,...,n_c\}\}$ can be collected, where the definition of $s_{(i,j)}$ is given in **Definition 1**. Scan $\{s_{(i,j)}\}$ and search for a T, that satisfies

$$s_{(0,T-1)} > s_{(1,T-1)} \quad \textit{and} \quad s_{(0,T)} < s_{(1,T)} \quad (6)$$

The collected $s_{(i,j)}$ from the 30 sampled patterns are shown in Table 1, which shows that Expression (6) is satisfied when $j = 3$, so T should be chosen as 3. Finally, the

Table 1: The collected values of $s_{(i,j)}$ from the 30 sampled BZ patterns

	$j=0$	$j=1$	$j=2$	$j=3$	$j=4$	$j=5$	$j=6$	$j=7$
$i=0$	180496	4720	2701	2061	760	107	19	1
$i=1$	587	937	1519	2922	2230	328	59	20

identified GHM for this example can be represented by:

$$c(x;y;t+1) = \begin{cases} (c(x;y;t)+1) \bmod 13 & \text{if } 1 \leq c(x;y;t) < 13 \\ 1 & \text{else if } \#(\mathcal{R}_{c(x;y;t)}) \geq 3 \\ 0 & \text{else} \end{cases} \tag{7}$$

4.4.3 Rule Identification using a Polynomial CA Model

According to the recent research in the identification of cellular automata a polynomial model [16], [17], of the form below, may be used to describe the BZ system

$$\begin{aligned} c(x;y;t) &= \theta_0 + \theta_1 c(x-a_1;y-b_1;t-1) + ... + \theta_m (c(x-a_1;x-b_1;t-1) \\ &\quad \times ... \times c(x-a_n;y-b_n;t-1)) \end{aligned} \tag{8}$$

where $c(x-a_1;y-b_1;t-1),...,c(x-a_n;y-b_n;t-1)$ denote the neighbourhood of the considered cell $c(x;y;t)$, and $\theta_i (i=0,...,m)$ represent the unknown parameters. Compared with previous studies of CA using polynomial models θ_i in Equation (8) can be real valued.

The neighbourhood was chosen as the Moore structure, with $N=13$ and $E=3$. The identification procedure for the BZ reaction based on Equation (8) can be summarized as:

1. Collect the input-output cases $\{x_i;y_i\}, i \in \{1,...,M\}$ using the neighbourhood and E, where M denotes the number of collected cases and n denotes the number of neighbourhood cells.

$$\begin{aligned} x_i &= \{c(x-a_1;y-b_1;t-1), c(x-a_2;y-b_2;t-1),...,c(x-a_n;y-b_n;t-1)\} \\ y_i &= c(x;y;t) \end{aligned} \tag{9}$$

2. Apply the Orthogonal Least Squares (OLS) algorithm for CA, first proposed by Billings in 1988 [20] and recently modified by Mei [21], to estimate the parameters

of Equation (8) using the collected data set $\{x_i; y_i\}$.

3. Because the Moore structure has 8 cells there will be $2^8 = 256$ potential terms in Equation (8). However, the Error Reduction Ratio (ERR), which is an inherent parameter of OLS can be used to describe the percentage contribution of each term to the updated cell. The candidate terms can then be ranked and the terms with the largest ERR can be included in the model and all other terms can be discarded. There is always a tradeoff between the model efficiency and the complexity of the model. In the current experiment, 30 terms produced a good model performance and predictions.

Following the procedure above the coefficients of all potential terms were estimated and 30 terms with the largest ERR were selected as the final terms, shown in Table 2.

4.4.4 Model Evaluation

We have shown that under normal experimental conditions that it is indeed possible to identify the evolution of the BZ reaction with CA models. To evaluate the identified models visually, Figure 13 shows the 12 time step predictions produced by Equation (7) and Equation (8). Both these clearly demonstrate the diffusion characteristics of the BZ patterns. To quantitatively access the performance of the obtained CA rules we can compare the results of the predictions from the identified models to the actual BZ evolution for a single time step. To achieve this a correlation coefficient, which takes into account the correct and false cell predictions for the excited state, and the correct and false cell predictions for other states will be used. The number of times that a cell with the excited state is predicted correctly can be denoted by e, while incorrect predictions will be denoted by $\bar{e}$. The number of times that a cell with other states is predicted correctly can be denoted by r, with incorrect predictions denoted by $\bar{r}$. The correlation coefficient, expressed by Equation(10) below, provides a measure of how well the rule predicted what actually occurred [22].

$$C = \frac{er - \bar{e}\bar{r}}{[(e+\bar{e})(e+\bar{r})(r+\bar{e})(r+\bar{r})]^{1/2}} \tag{10}$$

If the predicted behavior is always correct, then $C = 1$. If the predictions are always incorrect, then $C = -1$, and if the predictions are completely random, then $C = 0$.

Table 2: The selected 30 terms and coefficients of the polynomial model using OLS

	Term	θ_i	*ERR*
$i=1$	*constant*	0.31870	0.48391
$i=2$	$c(x;y-1)$	0.17200	0.02910
$i=3$	$c(x-1;y-1)*c(x-1;y+1)$	0.16594	0.01832
$i=4$	$c(x+1;y-1)*c(x+1;y+1)$	0.23040	0.01242
$i=5$	$c(x-1;y)*c(x;y+1)$	0.23187	0.00808
$i=6$	$c(x+1;y)*c(x;y+1)$	0.31333	0.00479
$i=7$	$c(x-1;y)$	−0.09860	0.00311
$i=8$	$c(x+1;y-1)*c(x+1;y)$	0.07244	0.00160
$i=9$	$c(x+1;y-1)*c(x+1;y)*c(x;y+1)*c(x+1;y+1)$	−0.19895	0.00135
$i=10$	$c(x-1;y)*c(x+1;y)*c(x-1;y+1)*c(x;y+1)$	−0.30327	0.00055
$i=11$	$c(x;y-1)*c(x-1;y)$	0.14632	0.00044
$i=12$	$c(x-1;y-1)*c(x+1;y)$	0.25643	0.00038
$i=13$	$c(x-1;y-1)*c(x;y-1)*c(x+1;y)$	−0.34056	0.00074
$i=14$	$c(x-1;y+1)*c(x;y+1)$	0.02263	0.00039
$i=15$	$c(x+1;y)*c(x-1;y+1)*c(x;y+1)*c(x+1;y+1)$	−0.19519	0.00046
$i=16$	$c(x+1;y+1)$	−0.08392	0.00043
$i=17$	$c(x-1;y+1)*c(x+1;y+1)$	0.12953	0.00042
$i=18$	$c(x;y-1)*c(x+1;y)$	0.13500	0.00038
$i=19$	$c(x;y-1)*c(x+1;y-1)*c(x+1;y)*c(x;y+1)$	−0.18413	0.00034
$i=20$	$c(x-1;y-1)*c(x-1;y)$	0.29123	0.00027
$i=21$	$c(x-1;y-1)*c(x-1;y)*c(x;y+1)$	−0.25805	0.00032
$i=22$	$c(x-1;y)*c(x-1;y+1)$	0.16316	0.00024
$i=23$	$c(x-1;y-1)*c(x+1;y-1)*c(x-1;y)*c(x+1;y)$	−0.21306	0.00025
$i=24$	$c(x-1;y-1)*c(x+1;y-1)$	0.15641	0.00028
$i=25$	$c(x-1;y-1)*c(x;y-1)*c(x+1;y-1)*c(x-1;y)$	−0.19384	0.00036
$i=26$	$c(x-1;y-1)$	−0.05866	0.00027
$i=27$	$c(x-1;y-1)*c(x;y+1)$	0.15614	0.00024
$i=28$	$c(x-1;y)*c(x-1;y+1)*c(x;y+1)*c(x+1;y+1)$	−0.24774	0.00024
$i=29$	$c(x-1;y)*c(x+1;y+1)$	0.14923	0.00023
$i=30$	$c(x-1;y-1)*c(x-1;y)*c(x-1;y+1)$	−0.16295	0.00017

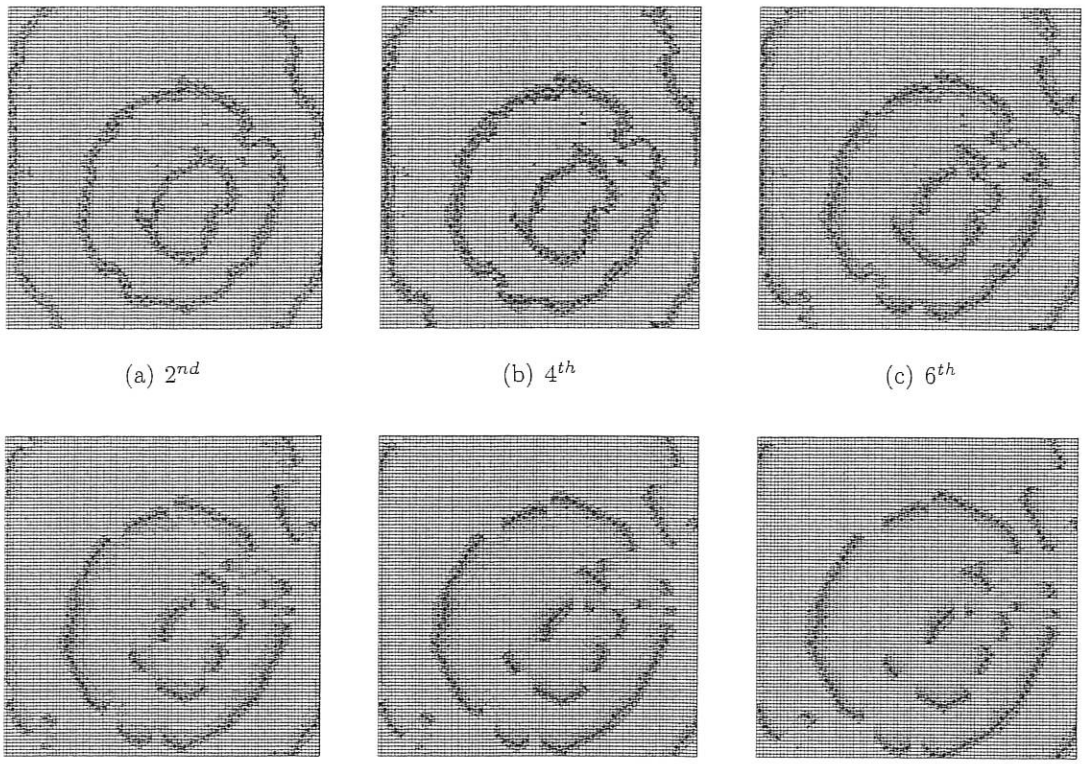

(a) 2^{nd} (b) 4^{th} (c) 6^{th}

(d) 8^{nd} (e) 10^{th} (f) 12^{th}

Figure 12: 12 time step ahead predictions produced by the identified GHM model - Equation (7)

Comparing the predictions from the identified GHM and polynomial model to the actual growth of BZ patterns for 4 step ahead predictions, the correlation coefficients are shown in Table 3. Table 3 shows the first 3 step predictions from both models are acceptable

Table 3: The correlation coefficients obtained through comparing the predictions from the identified GHM and polynomial model to the actual growth of BZ patterns for a 4 step predictions

Model	1^{st} step	2^{nd} step	3^{rd} step	4^{th} step
GHM	0.4436	0.3517	0.2096	-0.0269
Polynomial Model	0.4424	0.3503	0.2094	-0.0335

with a steady decline in the accuracy of predictions. The decreasing trend of the correlation coefficient will be due to accumulated prediction inaccuracies and/or noise on the nonlinear system. The correlation coefficient of the 4^{th} step prediction falls below zero indicating that the prediction may be suspect. One possible explanation for this appear-

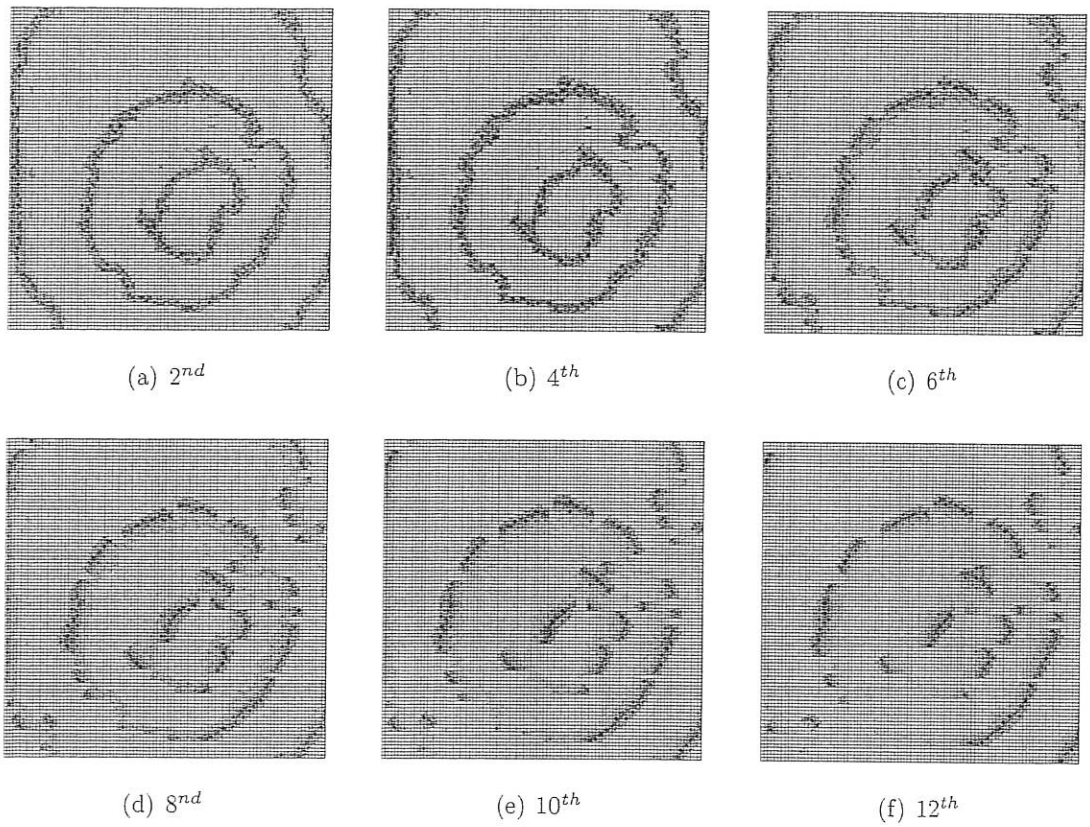

(a) 2^{nd} (b) 4^{th} (c) 6^{th}

(d) 8^{nd} (e) 10^{th} (f) 12^{th}

Figure 13: 12 time step ahead predictions produced by the identified polynomial model - Equation (8) and Table 2.

ance is that some new wave fronts are stimulated at this time step in the actual reaction, which are difficult to predict without any knowledge of the source of stimulation.
The results clearly show that the identified models do capture most of the features of the reaction patterns, such as the diffusion behavior of the wave fronts.

5 Conclusions

New methods of extracting mathematical models of CA directly from real imaged data from a BZ reaction has been presented. A procedure which maps the digital image to a latticed CA pattern has been proposed. New methods of synthesizing the horizontal and vertical calibration were introduced, together with edge purging procedure to remove the gradient between the wave fronts and the background. A new region selection approach was proposed, and procedures for the identification of two CA model types, the GHM and polynomial model, have been described. A comparison of the predictions with the actual

patterns both visually and quantitatively shows that the results are very encouraging. The identified models can reproduce the patterns with similar dynamic features compared to the actual BZ reaction.

Identification of real reaction systems is often very difficult because of the many factors involved. Moreover, natural data are will always be slightly corrupted by the imaging devices during data acquisition. The results in the paper represent preliminary results and many more experiments need to be conduced and all aspects of the data collection and modelling of this complex class of system require further study.

Acknowledgment

The authors gratefully acknowledge that part of this work was financed by EPSRC(UK).

References

[1] B.P.Belousov, *A Periodic Reaction and Its Mechanism*, Sbornik Referatov po Radiasionni Meditsine, Moscow, 1958.

[2] M.Zhabotinskii, "Periodic Kinetics of Oxidation of Malonic Acid in Solution (Study of the Belousov Reaction Kinetics)," *Biophys*, vol.9, pp.306-311, 1964.

[3] A.L.Hodgkin and A.F.Huxley, "A Quantitative Description of Membrane Current and its Application to Conduction and Excitation in Nerve," *J.Physical*, vol.117, pp.500-544, 1952.

[4] C.Luo and Y.Rudy, "A Dynamic Model of the Cardiac Ventricular Action Potential - Simulations of Ionic Currents and Concentration Changes," *Circulation Research*, vol.74, pp.1071-1097, 1994.

[5] R.J.Field and R.M.Noyes, "Oscillations in chemicals systems. IV. Limit cycle behaviour in a model of a real chemical reaction," *J. Chem. Phys*, vol.60, pp.1877-1884,1974.

[6] A.T.Winfree, "Spiral waves of chemical activity ", *Science*, vol.175, pp.634-636, 1972.

[7] D.Mollison, J.R.Stat, "Spatial contact models for ecological and epidemic spread,", *JRSS B*, vol.39, pp.283-326, 1977.

[8] A.J.Durston, J.Theor, "Dictyostelium discoideum aggregation fields as excitable media," *Biol.*, vol.42, pp.483-504, 1973.

[9] Andrew Adamatzky, *Cellular Automata: a discrete university,* World Scientific, London, 2001.

[10] Andersson C, Rasmussen S, White R, "Urban settlement transitions," *Enviroment and Planning B-Planning and Design*, vol.29, pp.841-865, 2002.

[11] Li XB, Jiang R, Wu QS, (2003), "Cellular automata model simulating complex spatiotemporal structure of wide jams," *Physical Review E*, 68(1) Part2,2003.

[12] Chaudhuri P.P., Chowdhury D. R., Nandi S, and Chattopadhyay S, *Additive Cellular Automata: Theory and Applications, IEEE Computer Society Press*, 1997.

[13] Greenberg,J.M., B.D.Hassard, and S.P.Hastings, "Pattern formation and periodic structures in systems modeled by reaction-diffusion equantions," *B.Am.Math.Soc.84*, pp.1296-1327, 1978.

[14] Robert Fisch, *Metastability in the Greenberg-Hasting Model, Annals of Applied Probability,* 1993

[15] Y.Zhao, S.A.Billings and Alex Routh, "Identification of Excitable Media using Cellular Automata," *Report of department of Automatic Control and Systems Engineering, University of Sheffield*, 897, 2005.

[16] Y.X.Yang and S.A.Billings, "Identification of probabilistic cellular automata," *IEEE Transactions on systems Man and Cybernetics Part B*, vol.33, no.2, pp.225-236, 2003.

[17] Y.X.Yang and S.A.Billings, "Identification of the neighbourhood and CA rules from spatio-temporal CA patterns," *IEEE Transactions on systems Man and Cybernetics Part B*, vol.30, no.2, pp.332-339, 2003.

[18] Y.Zhao, S.A.Billings, "Neighbourhood Detection Using Mutual Information for the Identification of Cellular Automata",*Accepted by IEEE Transactions on systems Man and Cybernetics Part B*, 2005.

[19] A.Adamatzky, Benjamin de Lacy Costello, "Experimental implementation of mobile robot taxis with onboard Belousov-Zhabotinsky chemical medium," *Material Science of Engineering Part C*, vol.24, pp.541-548, 2004.

[20] M.Korenberg, S.A.Billings, "Orthogonal parameter estimation algorithm for nonlinear stochastic systems," *International journal of control*, vol.48, no.1, pp.193-210, 1988.

[21] S.A.Billings, S.Mei, "A new fast cellular automata orthogonal least aquares identification method," *Report of AC&SE, University of Sheffield*, 2003.

[22] B.W.Mathews, "Comparison of the predicted and observed secondary structure of T4 phage lysozyme, " *Biochim. Biophys. Acta*, vol.405, pp.442-451, 1975.